

Phi-SegNet: Phase-Integrated Supervision for Medical Image Segmentation

Shams Nafisa Ali, *Student Member, IEEE* and Taufiq Hasan, *Senior Member, IEEE*

arXiv:2601.16064v1 [eess.IV] 22 Jan 2026

Abstract—Deep learning has substantially advanced medical image segmentation, yet achieving robust generalization across diverse imaging modalities and anatomical structures remains a major challenge. A key contributor to this limitation lies in how existing architectures—ranging from Convolutional Neural Networks (CNNs) to Transformers and their hybrids—primarily encode spatial information while overlooking frequency-domain representations that capture rich structural and textural cues. Although few recent studies have begun exploring spectral information at the feature level, supervision-level integration of frequency cues—crucial for fine-grained object localization—remains largely untapped. To this end, we propose *Phi-SegNet*, a CNN-based architecture that incorporates phase-aware information at both architectural and optimization levels. The network integrates *Bi-Feature Mask Former (BFMF)* modules that blend neighboring encoder features to reduce semantic gaps, and *Reverse Fourier Attention (RFA)* blocks that refine decoder outputs using phase-regularized features. A dedicated phase-aware loss aligns these features with structural priors, forming a closed feedback loop that emphasizes boundary precision. Evaluated on five public datasets spanning ultrasound, X-ray, histopathology, MRI, and colonoscopy, *Phi-SegNet* consistently achieved state-of-the-art performance, with an average relative improvement of $1.54 \pm 1.26\%$ in IoU and $0.98 \pm 0.71\%$ in F1-score over the next best-performing model. Additionally, in cross-dataset generalization scenarios involving unseen datasets from the known domain, *Phi-SegNet* exhibits robust and superior performance—highlighting its adaptability and modality-agnostic design. These findings demonstrate the potential of leveraging spectral priors in both feature representation and supervision, paving the way for generalized segmentation frameworks that excel in fine-grained object localization.

Index Terms—Medical image segmentation, deep learning, frequency domain, phase, reverse attention.

I. INTRODUCTION

MEDICAL image segmentation (MIS)—the task of identifying and delineating regions of interest such as organs, tumors, or lesions from medical images—plays a pivotal role in accurate diagnosis, treatment planning, and disease monitoring. However, manual segmentation demands

S. N. Ali and T. Hasan are with the mHealth Lab, Department of Biomedical Engineering, Bangladesh University of Engineering and Technology, Bangladesh, e-mail: {nafisa,taufiq}@bme.buet.ac.bd

S. N. Ali is also affiliated with the Department of Electrical and Computer Engineering, Johns Hopkins University, Baltimore, MD, USA.

T. Hasan has a secondary affiliation with the Center for Bioengineering Innovation and Design, Department of Biomedical Engineering, Johns Hopkins University, Baltimore, MD, USA.

substantial time and expert anatomical knowledge, resulting in high inter-observer variability and limited reproducibility. Consequently, there is an increasing demand for automated and reliable segmentation tools that can improve both the precision and throughput of clinical workflows.

Over the last decade, deep learning (DL) approaches, particularly those based on convolutional neural networks (CNNs), have significantly advanced MIS by learning rich feature hierarchies from data, outperforming traditional, hand-engineered methods. Among CNN-based architectures, U-Net [1] introduced a pivotal encoder-decoder framework with symmetric skip connections that fuse low-level spatial detail with high-level semantic context. However, the simplicity of U-Net limits its effectiveness when dealing with small or irregular structures, closely situated targets, fuzzy boundaries, and visually ambiguous regions. To address these challenges, numerous variants have been developed that incorporate multi-scale feature aggregation [2]–[4], redesigned skip pathways [5], and advanced attention mechanisms [6]–[9]. Building on these advances, CE-Net [10] and CPFNet [2] expanded the receptive field of the encoder through dense atrous convolution and multiscale context pooling, enabling more effective extraction of local and global semantic characteristics. Furthermore, models such as PraNet [11] and PRCNet [12] employ reverse attention to iteratively refine coarse predictions and enhance the delineation of ambiguous boundaries. Complementing these designs, dual-branch frameworks such as Twin-SegNet [13] improve segmentation consistency by jointly learning from both foreground and background perspectives.

Despite their success, CNNs are inherently limited by their localized receptive fields, which restrict their capacity to model long-range dependencies, crucial for understanding global anatomical context. This limitation has motivated the integration of transformer architectures in MIS. Early models like TransUNet [14] combine convolutional encoders with vision transformers to capture global relationships among features, while hybrid designs such as Transfuse [15], TransAttUNet [16], and H2Former [17] introduce hierarchical or scale-aware attention to enhance semantic consistency. These architectures have shown improved performance, particularly in complex anatomical scenes, but often demand large annotated datasets and rely heavily on spatial-domain cues.

As spatial-domain methods continue to dominate the field, frequency-domain modeling has recently emerged as a valuable complement by offering global signal representations through amplitude and phase decomposition. Techniques based

on Fourier or cosine transforms help highlight structural regularities, especially in noisy or low-contrast imaging conditions. Recent works such as MEW-UNet [18], FDFUNet [19], and GFUNet [20] leverage frequency filtering and spectral recalibration to enhance boundary delineation and reduce redundancy. Dual-domain networks like DBL-Net [21] and D²LNet [22] adopt parallel frequency and spatial encoders, fusing representations at multiple levels to better resolve semantic ambiguity. More recent approaches have explored explicit spectral attention and deeper spectral integration. SLf-UNet [23] introduces spectral recalibration units operating on frequency-transformed features to highlight relevant bands and suppress flat or noisy components, while tKFC-Net [24] applies twin-kernel frequency convolutions at each stage to balance global context with edge precision. Following this direction, BAWGNet [25] and LACFormer [26] exemplify spectral-domain-focused transformer architectures, embedding frequency-aware filtering directly into global attention pathways. However, most existing frequency-aware methods treat spectral processing as auxiliary—applying it post hoc or in isolated branches without integrating it actively into the learning process. They also tend to overlook phase-based guidance during training and do not leverage frequency-domain supervision to enhance structural consistency in the decoder. Moreover, current architectures rarely provide a feedback mechanism that connects decoder predictions with spectral properties, limiting their capacity to refine topology or suppress high-frequency noise during segmentation. These observations suggest the need for a more principled integration of spectral priors within the segmentation pipeline—ideally in a way that informs both attention formation and optimization dynamics during training.

To address these limitations, we propose **Phi-SegNet**, a frequency-aware segmentation framework that actively integrates spectral reasoning into the attention pathway and supervision process of the model. First, we introduce a *Bi-Feature Mask Former (BFMF)* module that modulates encoder features through learnable spectral and semantic fusion, promoting multi-scale integration. Second, to enhance the boundary refinement capability, we propose a *Reverse Fourier Attention (RFA)* mechanism that filters reverse attention maps in the frequency domain, selectively suppressing noise while preserving structure-aligned low-frequency content. Finally, we incorporate a novel *phase-integrated supervision loss*, which guides phase alignment between the prediction and ground truth masks in the Fourier domain, offering structure-aware training that complements pixel-wise loss functions. These three modules collectively enable Phi-SegNet to optimize jointly over spatial and spectral cues. Extensive evaluations across five distinct medical imaging modalities, i.e., ultrasound, X-ray, endoscopy, histology, and MRI, demonstrate the superiority of Phi-SegNet over state-of-the-art spatial and dual-domain models in both accuracy and boundary fidelity.

II. BACKGROUND

Fourier Transform offers a powerful means to analyze spatial patterns in images by decomposing them into frequency components, typically realized through its two-dimensional

discrete form. Let $x[m, n]$ be a grayscale image of size $M \times N$. The 2D DFT and its inverse are defined as:

$$X[k, l] = \sum_{m=0}^{M-1} \sum_{n=0}^{N-1} x[m, n] e^{-j(\frac{2\pi}{M} km + \frac{2\pi}{N} ln)} \quad (1)$$

$$x[m, n] = \frac{1}{MN} \sum_{k=0}^{M-1} \sum_{l=0}^{N-1} X[k, l] e^{j(\frac{2\pi}{M} km + \frac{2\pi}{N} ln)} \quad (2)$$

where $k = 0, 1, \dots, M - 1$ and $l = 0, 1, \dots, N - 1$.

Each Fourier coefficient $X[k, l]$ represents the frequency component corresponding to the spatial frequency index (k, l) . The *magnitude spectrum* characterizes the energy distribution of these frequency components, capturing texture patterns, intensity modulations, and dominant frequency bands, but it lacks spatial and structural localization. In contrast, the *phase spectrum* encodes the relative alignment of frequencies, preserving spatial structure, contour integrity, and geometric information within the image. Given the complex spectrum $X[k, l]$, the magnitude and phase spectra are respectively defined as:

$$|X[k, l]| = \sqrt{\Re\{X[k, l]\}^2 + \Im\{X[k, l]\}^2}, \quad (3)$$

$$\angle X[k, l] = \arctan\left(\frac{\Im\{X[k, l]\}}{\Re\{X[k, l]\}}\right). \quad (4)$$

Phase governs the spatial alignment of image structures in the frequency domain. When an image is translated, its magnitude spectrum remains unchanged, while the phase undergoes a linear shift. Let a two-dimensional image $f(x, y)$ have the Fourier transform $F(u, v)$:

$$F(u, v) = \iint f(x, y) e^{-j2\pi(ux+vy)} dx dy. \quad (5)$$

A translation by (x_0, y_0) produces a shifted image $f'(x, y) = f(x - x_0, y - y_0)$ with

$$F'(u, v) = F(u, v) e^{-j2\pi(ux_0+vy_0)}, \quad (6)$$

$$|F'(u, v)| = |F(u, v)|, \quad (7)$$

$$\angle F'(u, v) = \angle F(u, v) - 2\pi(ux_0 + vy_0). \quad (8)$$

Thus, spatial translation affects only the phase spectrum, confirming that phase information preserves positional and structural fidelity, whereas the magnitude spectrum reflects overall frequency content.

III. METHODOLOGY

A. Baseline Model

An encoder-decoder-based segmentation model with the EfficientNet-B4 [27] backbone has been selected as the baseline model for this work due to its excellent trade-off between performance and computational cost.

B. Proposed Phi-SegNet Architecture

1) *Encoder Pipeline*: The proposed **Phi-SegNet** architecture (illustrated in Fig. 1) employs an encoder pipeline that effectively extracts contextual representations relevant to the segmentation task across multiple feature levels. In this work, the input image $I_x \in \mathbb{R}^{H \times W \times 3}$ is passed through a pre-trained

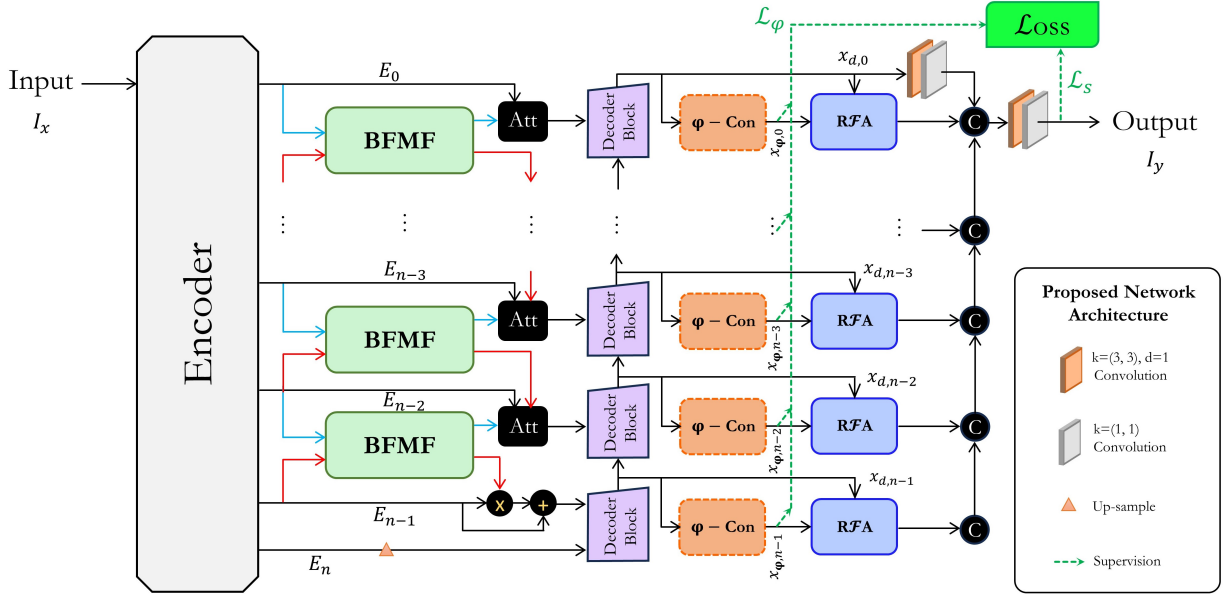


Fig. 1. Overview of the proposed Phi-SegNet. The architecture integrates encoder features via bi-feature mask former (BFMF) modules and attention-guided skip connections. Phase supervision is applied on decoder stages followed by reverse Fourier attention (RFA) modules, which use spectral filtering to enhance boundary localization.

EfficientNet-B4 encoder to obtain a set of hierarchical feature maps $\{E_0, E_1, \dots, E_n\}$, where each E_i represents the feature map at level i with its corresponding spatial resolution, and n denotes the total number of spatial hierarchy levels.

2) Bi-Feature Mask Former (BFMF) Module: The Bi-Feature Mask Former (BFMF) module integrates feature representations from two adjacent encoder levels, E_i and E_{i+1} , to enhance the fusion of semantic and spatial context. As illustrated in Fig. 1, the blue arrows feeding into the BFMF denote higher-resolution encoder features E_i , whereas the red arrows correspond to the adjacent lower-resolution encoder features E_{i+1} . In Fig. 2, we respectively denote these as x and x_s for notational simplicity.

Given $x \in \mathbb{R}^{H \times W \times C}$ and $x_s \in \mathbb{R}^{\frac{H}{2} \times \frac{W}{2} \times C_s}$, the module produces two corresponding mask features, y and y_s , at the same spatial scales. Multi-kernel convolutions (MkC) with varying kernel sizes ($k = \{1, 3, 5\}$) and dilation rates ($d = \{1, 2\}$) are employed to capture multi-scale receptive fields, as illustrated in Fig. 2. Features from higher dilation rates are processed less to better conserve their spatial dependencies. The operations are formulated as:

$$p_{11}, p_{21}, p_{31} = \text{MkC}(x), \quad (9)$$

$$x_{c1} = p_{11} \oplus p_{21} \oplus \text{Up}(x_s), \quad (10)$$

$$p_{12}, p_{22}, p_{32} = \text{MkC}(x_{c1}), \quad (11)$$

$$y = \sigma((p_{12} \oplus p_{22} \oplus p_{32}) * W_3^1 * W_1^1), \quad (12)$$

$$y_s = \text{Max}(\sigma(p_{32}) * W_1^1), \quad (13)$$

where W_k^d denotes a learnable weight tensor (k = kernel size, d = dilation rate), \oplus represents feature concatenation, σ is the sigmoid activation function, and $*$ indicates convolution.

The resulting mask features $y \in \mathbb{R}^{H \times W \times C}$ and $y_s \in \mathbb{R}^{\frac{H}{2} \times \frac{W}{2} \times C_s}$ are then passed through attention modules (Att) to

generate refined masks and further refine the encoded features $E_i \forall i \in [0, n-2]$.

To capture both fine-grained information and global context, the BFMF module leverages cascaded and dilated convolutions to expand the effective receptive field (RF) without additional parameters or resolution loss. Stacking three 3×3 convolutional layers (with stride 1 and padding) results in an effective RF of 7×7 , enabling hierarchical aggregation of local features. In contrast, a single 5×5 convolution with $d = 2$ achieves a receptive field of 9×9 , allowing it to directly access broader spatial context with fewer operations. By combining both strategies, BFMF benefits from a dual perspective: cascaded layers extract fine-grained details progressively, while dilated convolutions enhance global awareness through sparse, long-range connections. This design empowers the module to generate masks that encode both localized boundaries and long-range dependencies.

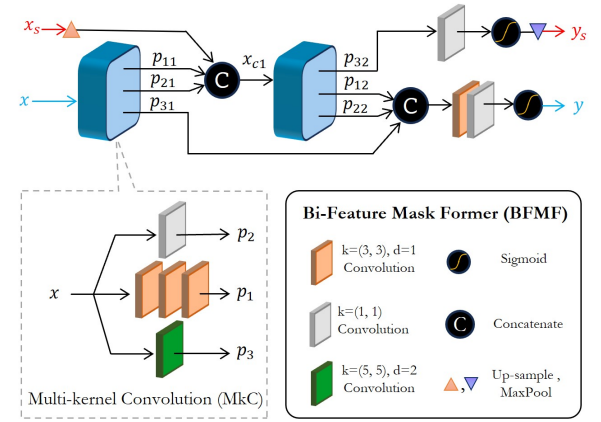


Fig. 2. The Bi-Feature Mask Former (BFMF) module extracts multi-scale semantic and spatial features through multi-kernel convolutions ($1 \times 1, 3 \times 3, 5 \times 5$) and sequential aggregation.

3) **Attention Module**: The attention modules (see Fig. 3) concatenate adjacent level features $y_s^{E_{i-1}}$ and y^{E_i} to extract spatial information which are optimum for refining the encoded quantity E_i . The generation of the refinement mask $E_{m,i}$ and the attention process can be shown as follows:

$$E_{m,i} = \sigma(BN(BN((y_s^{E_{i-1}} \oplus y^{E_i}) * W_3^1) * W_3^1)) \quad (14)$$

$$E_{A,i} = (E_i \otimes E_{m,i}) + E_i \quad (15)$$

where $BN(\cdot)$ indicates 2D-Batch Normalization, \otimes and $+$ denote the Hadamard product and element-wise summation, respectively.

4) **Decoder Module**: The decoder blocks take the output from the attention module, $E_{A,i}$, and concatenate it with the previous decoder output $x_{d,i+1}$. The concatenated features are then upsampled to match the resolution of the feature map at the current level, followed by a DoubleConv block to reconstruct spatial details and refine boundaries. Each DoubleConv block consists of two sequential convolutional layers, each with a kernel size of 3×3 , followed by Batch Normalization and a LeakyReLU activation function. This composition facilitates gradient flow and enhances the non-linearity required for accurate reconstruction.

$$x_{d,i} = \text{Up}(\text{DoubleConv}(E_{A,i} \oplus x_{d,i+1}))$$

The final output of each decoder stage is progressively passed through to gradually decode the segmentation mask.

5) **φ -Conditioner**: The phase (φ)-conditioner module, shown in Fig. 1, is designed to provide boundary-oriented supervision for the regions of interest. Each module consists of a single convolutional layer that projects multi-channel feature tensors into a single-channel representation, followed by a sigmoid activation. This yields feature-level boundary masks $x_{\varphi,i} \in [0, 1]^{H \times W \times 1}$ at each decoder level.

6) **Reverse Fourier Attention (RFA)**: To supervise the spatial quantities of the segmentation task, we utilize boundary information from the phase-conditioned masks x_{φ} and derive their reverse counterparts to emphasize the complementary foreground and background regions delineated by the boundary. The reverse mask is low-pass filtered in the frequency domain by retaining only a centered $\gamma \times \gamma$ region of low-frequency coefficients and setting the remaining components to zero. Such frequency-domain filtering is particularly effective in the early decoder stages, where feature maps are spatially coarse

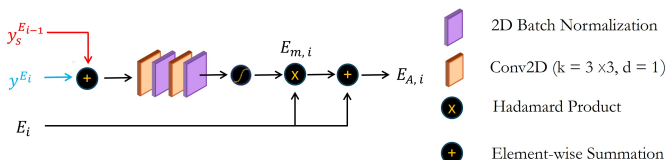


Fig. 3. Attention-guided fusion strategy. At each encoder stage E_i , the attention mask y^{E_i} is combined with the max-pooled mask from the preceding stage $y_s^{E_{i-1}}$, and passed through a convolutional block followed by a sigmoid activation to generate a refined attention map. This map modulates the encoder features via element-wise multiplication and is subsequently added to the decoder pathway.

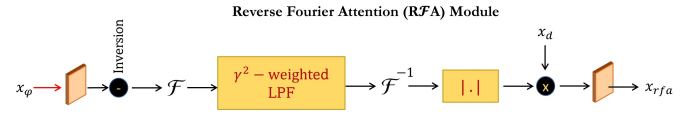


Fig. 4. The Reverse Fourier Attention (RFA) module applies a γ^2 -weighted low-pass filter in the frequency domain to enforce phase-conditioned boundary enhancement. Reverse attention focuses on what the model misses and helps it refine low-confidence regions like boundaries or tiny lesions. Early decoder features are coarse, applying LPF in Fourier space suppresses high-frequency noise, allowing attention to act on structurally dominant, globally coherent features.

and prone to high-frequency noise. The operations within the RFA module are defined as:

$$\hat{x}_{\varphi,i} = |\mathcal{F}^{-1}(\gamma^2 \otimes \mathcal{F}(1.0 - x_{\varphi,i}))| \quad (16)$$

where \mathcal{F} and \mathcal{F}^{-1} denote the Fourier and inverse Fourier Transforms, respectively; $|\cdot|$ indicates the absolute value; and γ is the scalar quantity controlling the cutoff of the low-pass filter (LPF). The resulting feature masks $\hat{x}_{\varphi,i}$ are subsequently combined with the decoder features $x_{d,i}$:

$$x_{rfa,i} = (x_{d,i} \otimes \hat{x}_{\varphi,i}) * W_3^1, \quad (17)$$

The outputs from all RFA modules are aggregated in the final layer to generate the prediction mask $I_y \in \mathbb{R}^{H \times W \times 1}$.

One of the core motivations behind the design of the RFA module is to facilitate complementary learning that explicitly refines the decoder's prediction by suppressing non-salient structures—particularly false positives in background regions. In conventional decoders, repeated fusion and upsampling operations often introduce spatial ambiguity. High-level features are spatially coarse, and their upsampled representations tend to leak into background areas. Although convolution and interpolation inherently behave as low-pass filters, their effects are implicit and uncontrolled, often failing to selectively suppress uncertain responses.

In contrast, the RFA module applies a deliberate, γ^2 -weighted LPF in the frequency domain on the residual between input and decoder prediction. This targeted filtering achieves two complementary refinements: (1) enforcing structural consistency by penalizing frequency-domain residuals between predicted and true boundaries, and (2) suppressing spurious activations in non-ROI regions while maintaining boundary sharpness. As a result, RFA guides the network to learn not only *what to activate* but also *what to suppress*, significantly reducing false positives and enhancing structural fidelity.

C. Phase-Integrated Loss Function

Phase information encapsulates the spatial localization and structural geometry of objects, making it crucial for delineating precise boundaries in segmentation tasks. To leverage this property, we impose a phase-alignment constraint between the φ -conditioned features and the corresponding ground-truth mask. Specifically, we enforce their 2D phase spectra to be consistent in the L_2 sense, thereby encouraging the predicted features to preserve boundary coherence in the frequency domain. However, the phase component of the Fourier transform

TABLE I

EFFECT OF VARYING LOSS HYPERPARAMETERS (α, β) ON SEGMENTATION PERFORMANCE USING THE BASELINE MODEL

α	β	BUSI		Kvasir-SEG	
		IoU	F1	IoU	F1
1	1	0.0897	0.1852	0.1455	0.3479
0.5	1	0.0766	0.1536	0.2394	0.4117
0.1	1	0.7066	0.8274	0.7104	0.8485
0.05	1	0.7158	0.8421	0.7463	0.8604
0.025	1	0.7284	0.8426	0.7582	0.8736
0.01	1	0.7460	0.8520	0.7658	0.8772
0.005	1	0.7258	0.8293	0.7505	0.8692

lies within the range $[0, 2\pi]$, introducing discontinuities and periodicity in the loss landscape. To mitigate this, the phase terms are unwrapped along both spatial axes prior to loss computation, ensuring that the supervisory signal increases smoothly as the prediction deviates spatially. The resulting phase-integrated loss is formulated as:

$$\varphi_{K,i} = \mathbf{u}[\angle x_{\varphi,i}; k]; \quad \varphi_{L,i} = \mathbf{u}[\angle x_{\varphi,i}; l]$$

$$\mathcal{L}_\varphi = \sum_{i=0}^{n-1} \left\| \varphi_{K,i} - \mathbf{u}[\angle I_y; k] \right\|_2 + \left\| \varphi_{L,i} - \mathbf{u}[\angle I_y; l] \right\|_2$$

where

$$\mathbf{u}[P; A] = \text{unwrap } P \text{ along A-axis}; \quad \|\cdot\|_2 = L_2\text{-Norm}$$

To supervise the spatial accuracy of the predicted mask, we adopt a conventional spatial loss (\mathcal{L}_s) based on the Intersection-over-Union (IoU) criterion:

$$\mathcal{L}_s = \frac{\sum_{h,w} I_y(h,w) \cdot \hat{I}_y(h,w)}{\sum_{h,w} I_y(h,w) + \hat{I}_y(h,w) - I_y(h,w) \cdot \hat{I}_y(h,w)} \quad (18)$$

The overall objective combines the phase-integrated supervision loss (\mathcal{L}_φ) and the spatial IoU loss (\mathcal{L}_s), forming the total loss:

$$\mathcal{L}_{\text{total}} = \alpha \mathcal{L}_\varphi + \beta \mathcal{L}_s \quad (19)$$

where α and β control the relative influence of phase- and spatial-domain supervision. Empirical tuning on the validation splits of the Kvasir-SEG and BUSI datasets (see Table I) revealed that overemphasizing the phase hyperparameter (α) caused underfitting in spatial representations, whereas underemphasizing it reduced the effectiveness of spectral regularization. The configuration ($\alpha = 0.01, \beta = 1.00$) achieved the best trade-off between boundary fidelity and overall segmentation accuracy, producing sharper object contours and fewer background activations across modalities, and was therefore adopted for all subsequent experiments.

IV. EXPERIMENTS AND RESULTS

A. Datasets

We conduct experiments on five benchmark tasks involving segmentation of breast lesions (BUSI, Mendeley, UDIAT), teeth (TDD), polyps (Kvasir-SEG, CVC-ColonDB), colorectal glands (GLaS), and prostate (PROMISE-12) from medical

images, spanning five widely used imaging modalities such as ultrasound (US), X-ray, colonoscopy, histopathology, and magnetic resonance imaging (MRI). These datasets collectively represent diverse clinical scenarios and modality-specific challenges, including intra-patient variability and heterogeneous acquisition conditions in ultrasound, complex anatomical and textural patterns in dental radiographs, high illumination and morphological variability in endoscopy, stain and tissue heterogeneity in histopathology, and inter-scanner domain shifts in MRI. To evaluate cross-domain robustness, the Mendeley, UDIAT, and CVC-ColonDB datasets are excluded from training and used solely for external validation. For datasets with official splits provided by their organizers (e.g., GLaS and PROMISE-12), those partitions are followed. Otherwise, images are randomly divided into training, validation, and test subsets in an 8:1:1 ratio. All experiments follow identical pre-processing, training, and evaluation protocols. A summary of the datasets is presented in Table II.

B. Experimental Setup

1) Implementation Details: All experiments have been implemented using PyTorch 2.3.0 with CUDA 12.1 and conducted on an Ubuntu 20.04 workstation equipped with four NVIDIA GeForce RTX 2080 Ti GPUs (11 GB each), an Intel® Core™ i9-7920X CPU @ 2.90 GHz, and 125 GB of RAM.

The input images are resized to 256×256 pixels. Data augmentation strategies included random horizontal and vertical flips, as well as affine transformations with translation. A multi-scale training strategy $\{0.5, 1.25\}$ is also employed for effectively enforcing scale invariance [11]. The model is trained for 150 epochs using the Adam optimizer with an initial learning rate of 1×10^{-5} with a batch size of 4. A cosine annealing learning rate scheduler is applied with $T_{\text{max}} = 25$ and $\eta_{\text{min}} = 1 \times 10^{-7}$. Model weights corresponding to the lowest validation loss have been retained.

2) Evaluation Metrics: To comprehensively and objectively assess the proposed architecture, Intersection over Union (IoU) has been employed as the primary evaluation metric. Additionally, Dice similarity index (DICE), pixel-wise accuracy (ACC), precision (PRE), recall (REC), F1-score (F1), and average symmetric surface distance (ASDD) are reported.

TABLE II
SUMMARY OF THE DATASETS USED

Dataset	Modality	Total	Train	Val	Test
†BUSI [28]	Breast US	647	517	65	65
‡TDD [29]	Dental X-ray	1000	800	100	100
Kvasir-SEG [30]	Colonoscopy	1000	800	100	100
GLaS [31]	Histopathology	165	72	13	80
§PROMISE-12 [32]	Prostate MRI	1473	778	277	418
UDIAT [33]	Breast US	163	—	—	163
Mendeley [34]	Breast US	250	—	—	250
CVC-ColonDB [35]	Colonoscopy	380	—	—	380

† From the 780 images of BUSI, only the 647 lesion-containing samples are used.

‡ Only the tooth-level annotations from the TDD are used.

§ Only the extracted 2D axial slices containing the prostate region are considered from PROMISE-12.

TABLE III

QUANTITATIVE COMPARISON OF SEGMENTATION PERFORMANCE ON BUSI AND TUFTS DENTAL DATASET (TDD). BEST, SECOND-BEST, AND THIRD-BEST SCORES ARE HIGHLIGHTED IN **RED**, **BLUE**, AND **BROWN**, RESPECTIVELY.

Methods	BUSI							TDD						
	IoU↑	DICE↑	ACC↑	PRE↑	REC↑	FI↑	ASSD↓	IoU↑	DICE↑	ACC↑	PRE↑	REC↑	FI↑	ASSD↓
UNet [1]	0.6583	0.7618	0.9485	0.8275	0.7666	0.7958	4.0041	0.7731	0.8736	0.9723	0.8955	0.8641	0.8794	1.0549
UNet++ [5]	0.7614	0.8426	0.9643	0.8934	0.8402	0.8662	2.6828	0.8049	0.9215	0.9809	0.9085	0.9183	0.9120	0.8811
ResUNet++ [36]	0.7881	0.8764	0.9688	0.8719	0.8979	0.8847	2.1816	0.8239	0.8952	0.9790	0.8918	0.9194	0.9053	0.8040
CE-Net [10]	0.8217	0.8799	0.9765	0.8964	0.9171	0.9066	1.8718	0.8335	0.9200	0.9803	0.9066	0.9349	0.9205	0.7656
CPFNet [2]	0.8074	0.8738	0.9727	0.8841	0.9018	0.8720	2.0494	0.8353	0.9217	0.9811	0.9199	0.9247	0.9222	0.7602
PraNet [11]	0.7819	0.8512	0.9704	0.8576	0.9132	0.8845	2.3526	0.7547	0.8668	0.9654	0.8234	0.9184	0.8683	4.5301
Y-Net [37]	0.7721	0.8603	0.9629	0.8753	0.8753	0.8752	2.3571	0.7916	0.9162	0.9796	0.9016	0.9328	0.9169	0.8853
AAU-Net [9]	0.7930	0.8570	0.9657	0.8768	0.8911	0.8838	2.2345	0.8150	0.9169	0.9800	0.9056	0.9291	0.9176	0.7787
MEW-UNet [18]	0.8059	0.8599	0.9742	0.8939	0.9101	0.9016	1.9447	0.8287	0.9163	0.9792	0.8994	0.9349	0.9168	1.0137
TransAttUNet [16]	0.7627	0.8480	0.9628	0.8503	0.8932	0.8712	2.6033	0.8385	0.9177	0.9816	0.9068	0.9367	0.9215	0.7463
Twin-SegNet [13]	0.8145	0.8862	0.9751	0.8765	0.9075	0.8917	1.8523	0.8487	0.9293	0.9153	0.8969	0.9410	0.9184	1.4607
Phi-SegNet	0.8454	0.9147	0.9806	0.9290	0.9108	0.9198	1.4999	0.8537	0.9329	0.9831	0.9258	0.9412	0.9334	0.6773

C. Comparison With SOTA Methods

To assess the performance of the proposed Phi-SegNet, a comprehensive quantitative evaluation has been conducted against eleven state-of-the-art deep learning segmentation architectures (summarized in Tables III–V). The benchmark encompasses a diverse spectrum of representative segmentation paradigms, including foundational convolutional models such as UNet [1], UNet++ [5], and ResUNet++ [36]; advanced spatial-domain architectures such as CE-Net [10], CPFNet [2], PraNet [11], AAU-Net [9], and Twin-SegNet [13]; spectral-domain models such as MEW-UNet [18] and the dual-domain Y-Net [37]; as well as hybrid CNN–Transformer frameworks exemplified by TransAttUNet [16]. To ensure fairness and consistency, all competing methods have been reimplemented (adapting from their official codebases) and trained under a unified data augmentation and optimization protocol across the five datasets. Complementing these quantitative evaluations, Fig. 5 presents qualitative comparisons of Phi-SegNet against five top-performing models, demonstrating its superior boundary adherence and structural fidelity.

1) *Evaluation on Breast Lesion Segmentation*: As shown in Table III, Phi-SegNet achieves state-of-the-art performance on the BUSI dataset, attaining the highest IoU and F1-score of 84.54% and 91.98%, respectively. Compared to the second-best performing model, CE-Net, our model yields consistent improvements across all metrics (except recall), with a gain of +2.37% in IoU, +1.32% in F1, while reducing the ASDD from 1.8718 to 1.4999.

From a visual standpoint, Fig. 5(a) illustrates that several competing models struggle to accurately capture the complex outer contour of the malignant lesion. CENet, CPFNet, and MEWUNet undersegment the tumor, leaving large portions of the irregular boundary unaccounted for. TransAttUNet and Twin-SegNet over-segment the lesion by smoothing across concavities, ignoring localized boundary indentations. In contrast, Phi-SegNet achieves the best visual alignment with the ground truth, precisely tracing the jagged tumor edges. Notably, it is the only model to maintain contour continuity along the left and lower borders without leaking into adjacent tissues. As shown in Fig. 5(b), all models perform comparably for the benign case, which is structurally well defined and visually distinguishable. These observations highlight Phi-

SegNet’s robustness in capturing heterogeneous lesion boundaries in breast ultrasound images.

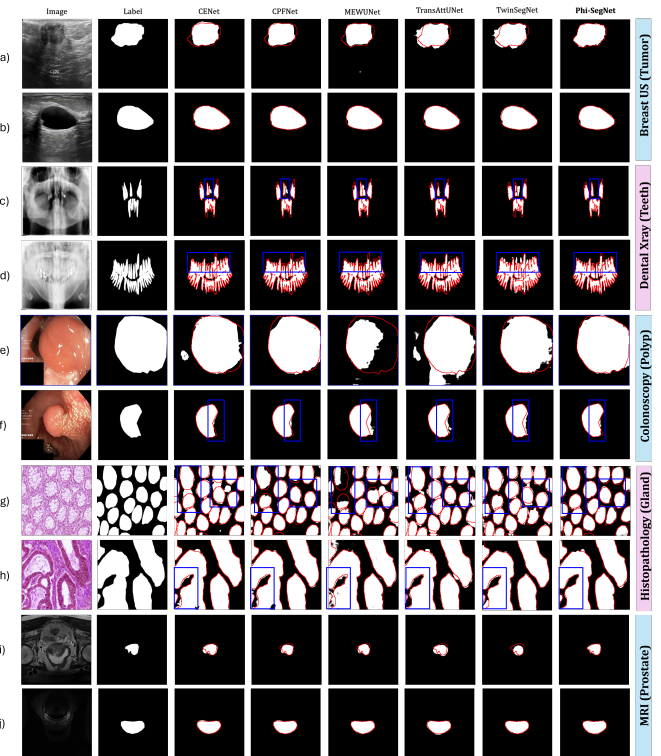


Fig. 5. Visualization of segmentation results obtained by Phi-SegNet and other state-of-the-art architectures (two test cases from each dataset). Certain regions in some of the images have been marked using blue bounding boxes to highlight the differences for the convenience of the reader.

2) *Evaluation on Teeth Segmentation*: Achieving the lowest ASSD score of 0.6733, Phi-SegNet demonstrates almost perfect boundary delineation. The quantitative representation in Table III further reveals that it achieves the best IoU and F1 scores of 85.37% and 93.34%, respectively (+0.50% and +1.50% higher than Twin-SegNet in terms of IoU and F1, respectively). Qualitatively, Fig. 5(c)–(d) present two challenging samples with crowded tooth arrangements and narrow inter-tooth spacing. Most models fail to capture sharper crown contours, especially around the cusp region in Fig. 5(c).

TABLE IV

QUANTITATIVE COMPARISON OF SEGMENTATION PERFORMANCE ON KVASIR-SEG AND GLAS DATASETS. BEST, SECOND-BEST, AND THIRD-BEST SCORES FOR EACH METRIC ARE HIGHLIGHTED IN **RED**, **BLUE**, AND **BROWN**, RESPECTIVELY.

Methods	Kvasir-SEG							GLaS						
	IoU↑	DICE↑	ACC↑	PRE↑	REC↑	FI↑	ASSD↓	IoU↑	DICE↑	ACC↑	PRE↑	REC↑	FI↑	ASSD↓
UNet [1]	0.6433	0.7566	0.9266	0.8211	0.7754	0.7976	5.3399	0.5114	0.6598	0.5118	0.5108	0.5185	0.6767	68.4656
UNet++ [5]	0.7465	0.8344	0.9490	0.8368	0.8936	0.8642	3.1446	0.7900	0.8543	0.8801	0.8451	0.7395	0.8897	3.3494
ResUNet++ [36]	0.7140	0.8014	0.9399	0.8398	0.8538	0.8467	3.9315	0.7109	0.8162	0.8297	0.8496	0.8282	0.8387	4.2321
CE-Net [10]	0.8032	0.8701	0.9637	0.9123	0.8866	0.8982	2.5477	0.8253	0.8991	0.9002	0.9231	0.8891	0.9057	2.3485
CPFNet [2]	0.8162	0.8794	0.9653	0.9013	0.9053	0.9033	2.9053	0.8287	0.9056	0.9075	0.9064	0.9141	0.9102	2.9475
PraNet [11]	0.7550	0.8377	0.9471	0.8490	0.8932	0.8709	3.8235	0.6726	0.8036	0.7791	0.7367	0.9115	0.8148	16.9096
Y-Net [37]	0.7254	0.8170	0.9424	0.8595	0.8411	0.8501	3.9857	0.7450	0.8478	0.8614	0.8829	0.8553	0.8688	3.6409
AAU-Net [9]	0.7584	0.8351	0.9487	0.8622	0.8667	0.8644	3.4935	0.7637	0.8627	0.8712	0.8747	0.8783	0.8765	3.3333
MEW-UNet [18]	0.7753	0.8540	0.9516	0.8968	0.8708	0.8835	3.1729	0.7787	0.8685	0.8747	0.8825	0.8806	0.8792	3.3747
TransAttUNet [16]	0.7746	0.8557	0.9658	0.8761	0.8920	0.8840	2.6258	0.8053	0.8866	0.8889	0.8673	0.9270	0.8961	3.2690
Twin-SegNet [13]	0.8109	0.8826	0.9648	0.8731	0.9185	0.8934	2.2324	0.8254	0.9006	0.9007	0.8793	0.9330	0.9053	2.8476
Phi-SegNet	0.8496	0.9117	0.9761	0.9185	0.9264	0.9224	1.7547	0.8383	0.9096	0.9079	0.9068	0.9243	0.9149	2.3477

While Twin-SegNet produces a visually clean mask, it under-segments the region near the lower premolars and introduces false positives around the upper incisors. Similarly, in Fig. 5(d), an oversegmentation artifact is clearly visible in the upper incisor region of Twin-SegNet’s output. Phi-SegNet, on the other hand, demonstrates the highest fidelity to the ground truth in both cases, maintaining intricate boundaries and sharp anatomical edges.

3) Evaluation on Polyp Segmentation: As reported in Table IV, Phi-SegNet achieves the best segmentation performance on the Kvasir-SEG dataset, with an IoU of 84.96%, F1-score of 92.24%, and the lowest ASSD of 1.7547. Compared to the second-best model, CPFNet, which records 81.62% IoU and 90.33% F1-score, our model offers an improvement of +3.34% in IoU and +1.91% in F1, while further reducing ASDD by 1.1506. The visual assessment in Fig. 5(e)–(f) further corroborates these findings for the polyp segmentation task. Both samples present challenging cases with polyps occupying most of the field of view and showing minimal morphological separation from the surrounding mucosa. Specifically, the boundary between the distal margin of the polyp and the mucosal fold appears visually continuous, leading to MEW-UNet and Twin-SegNet undersegmenting along the right lateral borders whereas TransAttUNet introduces significant spatial leakage along the edges. Phi-SegNet, however, produces more restrained and anatomically plausible masks with superior localization and refined boundary adherence, effectively resolving structural ambiguities under low-contrast conditions.

4) Evaluation on Gland Segmentation: As reported in Table IV, Phi-SegNet achieves the highest F1-score (91.49%) and IoU (83.83%) on the GLaS dataset, along with competitive precision (90.58%) and recall (92.43%) scores. In both Fig. 5(g)–(h), we observe that most models, including CE-Net, MEW-UNet, and Twin-SegNet, struggle to maintain boundary separation between closely located gland instances. These issues are especially prominent in the boxed regions (blue), where gland boundaries become blurred or collapse entirely. Although TransAttUNet and CPFNet perform relatively better, their boundary delineation remains inconsistent with noticeable pixel gaps. In contrast, Phi-SegNet demonstrates its superiority in the challenging histopathological task by resolv-

ing ambiguous gland boundaries and producing anatomically precise masks.

5) Evaluation on Prostate Segmentation: On the PROMISE-12 dataset, Phi-SegNet achieves the best performance with an IoU of 83.62%, F1-score of 91.50%, and the lowest ASSD of 0.8926, outperforming CPFNet by +0.54% IoU and +0.40% F1 (see Table V). Visual assessment in Fig. 5(i)–(j) reinforces these findings. In Fig. 5(i), the prostate exhibits a compact, bean-shaped structure with a subtle indentation along the left margin, where weak boundary contrast causes most models to deviate. Twin-SegNet and CPFNet undersegment the lateral regions, whereas TransAttUNet and CE-Net slightly overshoot inferiorly. Fig. 5(j) shows a more regular morphology where most models perform reasonably well but still display minor boundary inconsistencies. Phi-SegNet, however, produces smooth and anatomically coherent contours with minimal leakage in both cases, preserving fine structural details and demonstrating robustness to low contrast and intensity inhomogeneity in pelvic MRI scans.

TABLE V

QUANTITATIVE COMPARISON OF SEGMENTATION PERFORMANCE ON THE PROMISE-12 DATASET. BEST, SECOND-BEST, AND THIRD-BEST SCORES ARE HIGHLIGHTED IN **RED**, **BLUE**, AND **BROWN**, RESPECTIVELY.

Methods	IoU↑	DICE↑	ACC↑	PRE↑	REC↑	FI↑	ASSD↓
UNet [1]	0.6924	0.7976	0.9898	0.8129	0.8369	0.8247	1.8001
UNet++ [5]	0.8231	0.8966	0.9949	0.8773	0.9211	0.9031	0.9851
ResUNet++ [36]	0.8186	0.8945	0.9949	0.8824	0.9251	0.9037	0.9932
CE-Net [10]	0.8293	0.9015	0.9952	0.8947	0.9261	0.9096	0.9505
CPFNet [2]	0.8308	0.9029	0.9956	0.9161	0.9064	0.9110	0.9295
PraNet [11]	0.8037	0.8867	0.9954	0.9006	0.9068	0.9037	0.9305
Y-Net [37]	0.8203	0.8940	0.9950	0.8994	0.9099	0.9046	0.9959
AAU-Net [9]	0.8263	0.8885	0.9953	0.8609	0.9228	0.8913	0.9573
MEW-UNet [18]	0.8186	0.8942	0.9953	0.8769	0.9325	0.9038	1.0170
TransAttUNet [16]	0.8256	0.8978	0.9957	0.9050	0.9252	0.9140	0.9300
Twin-SegNet [13]	0.8264	0.8972	0.9951	0.8766	0.9380	0.9062	0.9819
Phi-SegNet	0.8362	0.9055	0.9965	0.9058	0.9289	0.9150	0.8926

D. Evaluation of Generalization

To assess the generalization capability of Phi-SegNet, we have trained a unified model (Phi-Seg_{gen}) on a combined dataset encompassing the first five datasets listed in Table II. Its performance has been evaluated both on the merged test set and on each individual test set.

TABLE VI

PERFORMANCE OF PHI-SEGNET_{GEN}. TRAINED ON THE MERGED DATASET, RESULTS REPORTED FOR THE MERGED TEST SET AS WELL AS THE INDIVIDUAL TEST SETS

Dataset	IoU↑	DICE↑	ACC↑	PRE↑	REC↑	F1↑	ASSD↓
BUSI	0.7936	0.8681	0.9748	0.9061	0.8725	0.8681	0.2443
Kvasir-SEG	0.7835	0.8611	0.9576	0.8776	0.8962	0.8611	3.1044
TDD	0.8324	0.9197	0.9800	0.9211	0.9194	0.9197	0.6909
GLaS	0.6369	0.7704	0.8065	0.9209	0.6776	0.7704	6.2019
PROMISE-12	0.8036	0.8841	0.9944	0.8910	0.9021	0.8841	1.1165
Merged	0.7897	0.8752	0.9674	0.8987	0.8809	0.8752	1.8546

TABLE VII

UNSEEN CROSS-DATASET EVALUATION OF PHI-SEGNET USING GENERALIZED AND MODALITY-SPECIFIC WEIGHTS

Dataset	Variant	IoU↑	DICE↑	ACC↑	PRE↑	REC↑	F1↑	ASSD↓
UDIAT	Phi-Seg _{gen}	0.7043	0.7899	0.9823	0.7825	0.8764	0.7901	2.0798
	Phi-Seg _{BUSI}	0.7796	0.8561	0.9876	0.8206	0.9168	0.8562	1.5046
Mendeley	Phi-Seg _{gen}	0.1821	0.2114	0.8702	0.5740	0.2107	0.2115	12.7983
	Phi-Seg _{BUSI}	0.6261	0.7261	0.9383	0.8490	0.7358	0.7261	5.2476
CVC Colon-DB	Phi-Seg _{gen}	0.5423	0.6214	0.9601	0.8039	0.6364	0.6215	3.9703
	Phi-Seg _{Kvasir}	0.5932	0.6622	0.9633	0.8341	0.6715	0.6622	3.5241

As summarized in Table VI, Phi-Seg_{gen} achieves a mean IoU of 78.97% and Dice score of 87.52% on the merged test set across modalities, indicating strong generalization without task-specific fine-tuning. Its performance closely follows that of dataset-specific trained models on TDD and PROMISE-12 and remains competitive on BUSI and Kvasir-SEG. Nevertheless, a noticeable drop is observed for GLaS (IoU = 63.69%), likely due to its limited representation ($\approx 2.5\%$ of training data).

E. Unseen Cross-Dataset Evaluation

To evaluate robustness beyond the training distribution, we have performed cross-dataset testing on three unseen datasets—UDIAT, Mendeley, and CVC-ColonDB. For each target domain, two variants are compared: the generalized model (Phi-Seg_{gen}) trained on all modalities, and the modality-specific model (e.g., BUSI for ultrasound, Kvasir-SEG for colonoscopy). As shown in Table VII, modality-specific weights consistently yield superior segmentation across all datasets, confirming the perception that domain-relevant knowledge enhances performance. Despite having no prior exposure to the target datasets, **Phi-Seg_{BUSI}** and **Phi-Seg_{Kvasir}** maintain fair segmentation quality, indicating that the network effectively learns transferable structural priors such as lesion morphology and boundary continuity.

V. DISCUSSION

A. Ablation Studies

To evaluate the contribution of each architectural component, we conducted a series of ablation studies on the BUSI dataset. Starting from a baseline with an EfficientNet-B4 encoder-decoder and spatial loss (\mathcal{L}_s), we progressively introduced phase supervision loss (\mathcal{L}_φ), Bi-Feature Mask Former (BFMF) modules, inter-level attention blocks, and Reverse Fourier Attention (RFA) modules to quantify their individual and combined effects. The corresponding model variants and results are summarized in Table VIII.

TABLE VIII

ABLATION STUDY ON BUSI (TEST SET) SHOWING THE EFFECT OF ARCHITECTURAL MODULES AND LOSS COMPONENTS

Model Variant	\mathcal{L}_s	\mathcal{L}_φ	IoU	F1
Baseline (EfficientNetB4)	✓		0.7792	0.8574
Baseline (EfficientNetB4)	✓	✓	0.7905	0.8672
Baseline + BFMF	✓		0.8170	0.9037
Baseline + BFMF	✓	✓	0.8293	0.9106
Baseline + BFMF + Att	✓	✓	0.8362	0.9150
Baseline + BFMF + Att + RFA ($\gamma=3$)	✓	✓	0.8454	0.9198

*Whenever \mathcal{L}_φ contributes to the total loss, φ -Conditioner is also present in the architecture to prepare the corresponding phase masks.

1) Effect of Incorporating Phase Supervision Loss (\mathcal{L}_φ):

Comparing the baseline (Row 1) with its phase-supervised counterpart (Row 2) in Table VIII, an increase in IoU from 0.7792 to 0.7905 and F1 from 0.8574 to 0.8672 can be observed, clearly indicating improved structural delineation. A similar absolute gain (+1.23% IoU, +0.69% F1) is observed when \mathcal{L}_φ is applied on the BFMF-embedded baseline architecture (Row 3 vs. Row 4). These results confirm that phase supervision provides complementary boundary-aware guidance to spatial-domain learning.

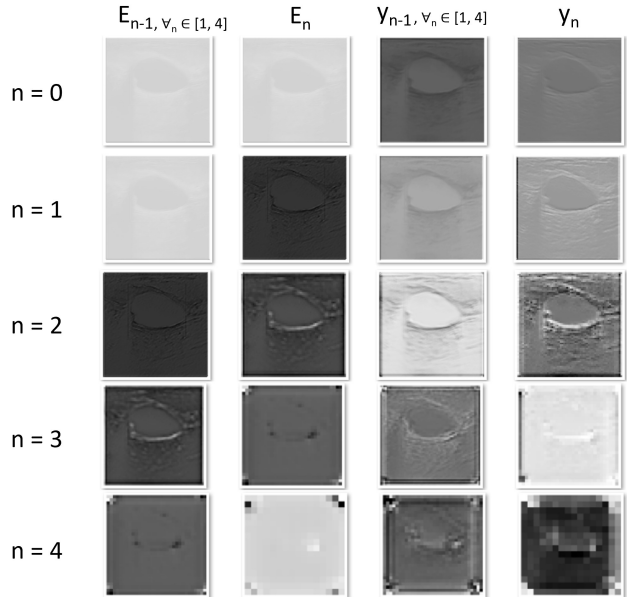


Fig. 6. Visualization of BFMF feature maps (single-channel). From left to right: input features from E_{n-1} (higher resolution), E_n (lower resolution), and the corresponding BFMF outputs y_{n-1} and y_n . Here, n denotes the encoder level, with $n = 0$ indicating the highest spatial resolution. All feature maps have been rescaled to 256×256 for better perception. Lesions appear more prominent in the fused outputs, demonstrating the effectiveness of BFMF.

2) Effect of Incorporating BFMF Modules: As shown in Table VIII, integrating BFMF modules to the baseline significantly boosts performance, with IoU increasing from 0.7792 to 0.8170 and F1-score from 0.8574 to 0.9037. Under phase supervision (Row 2 vs. Row 4), a similar IoU gain (+3.88%) is observed, confirming that BFMF effectively bridges the semantic gap between shallow and deep encoder features.

TABLE IX

IMPACT OF FOURIER FILTER TYPES AND γ PARAMETERS IN RFA.
RESULTS ARE REPORTED ON BUSI (VALIDATION SET)

Model Variant	IoU	F1
Phi-SegNet Core + RFA (No filter)	0.7538	0.8380
Phi-SegNet Core + RFA (HPF: $\gamma = 3$)	0.7442	0.8235
Phi-SegNet Core + RFA (Leaky LPF: $\gamma = 3$)	0.7642	0.8474
Phi-SegNet Core + RFA (LPF: $\gamma = 3$)	0.7956	0.8662
Phi-SegNet Core + RFA (LPF: $\gamma = 5$)	0.7917	0.8639
Phi-SegNet Core + RFA (LPF: $\gamma = 9$)	0.7881	0.8609

through multi-kernel contextual fusion. Fig. 6 offers a visual justification of the behavior of BFMF. From the intermediate feature maps, it can be observed that compared to the encoders (E_n , E_{n-1}), the outputs of the BFMF (y_n and y_{n-1}) depict enhanced contrast and better lesion focus, indicating successful modulation and feature refinement.

3) Effect of Incorporating RFA Modules: The Reverse Fourier Attention (RFA) modules guide decoder features through frequency-domain modulation using a simple 3×3 low-pass filter (LPF). While high-pass filtering (HPF) might intuitively seem favorable for enhancing edge details, our experiments revealed the opposite (see Table IX). HPF degraded performance (IoU: 0.7442), likely amplifying high-frequency noise present in early decoder stages. To explore smoother spectral transitions, we also implemented a leaky γ -weighted LPF defined as:

$$\Gamma(k, l) = \left(1 + \sqrt{\frac{k^2 + l^2}{M^2 + N^2}}\right)^{-\gamma}, \quad \gamma > 0,$$

which gradually attenuates high-frequency components instead of imposing an abrupt cutoff. Although this formulation demonstrated marginal improvement (IoU: 0.7642), the standard LPF achieved the best performance (IoU: 0.7956, F1: 0.8662). This can be attributed to the effective suppression of high-frequency disturbances by the LPF, resulting in better structural clarity in downstream feature refinement. This hypothesis is visually supported in Fig. 7, which presents the saliency maps produced by RFA ($\gamma = 3$) at multiple decoder depths. While RFA₄ generates diffuse and noisy responses, progressively shallower modules (e.g., RFA₀) exhibit sharper lesion boundaries and more localized attention.

Further analysis was conducted to assess the sensitivity of LPF to different γ values ($\gamma = \{3, 5, 9\}$). As shown in Table IX, $\gamma = 3$ appeared to be the optimal setting achieving the most balanced trade-off between structure preservation and noise suppression. Larger γ values expanded the retained region but led to excessive smoothing, weakening critical boundary definitions. Overall, these findings underscore the importance of controlled frequency-domain modulation in phase-integrated learning pipelines, where both over-suppression and over-inclusion of spectral components can adversely affect segmentation fidelity.

B. Computational Complexity

As reported in Table X, Phi-SegNet contains 59.72M parameters and requires 81.91 GFLOPs per forward pass, with an

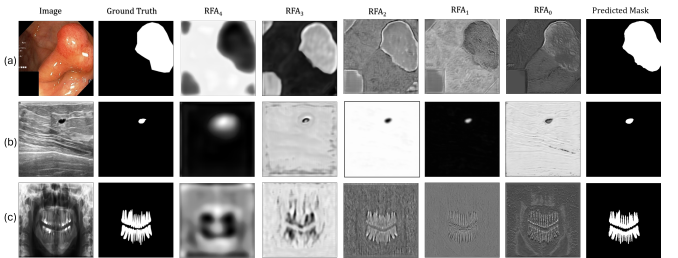


Fig. 7. Feature maps from RFA across decoder stages ($n = 4$ to 0) in the final PhiSegNet. As decoding progresses, spatial resolution increases and feature refinement improves significantly—culminating in sharper boundary localization at RFA₀.

average inference time of 44.41 ms. Although the parameter count exceeds that of most compared models, the increase arises from its joint spatial–frequency modeling and multi-scale aggregation in the BFMF modules. Compared to MEW-UNet and TransAttUNet, which rely on heavy backbones or full self-attention, Phi-SegNet achieves a notably better trade-off between accuracy and complexity. Architectures such as CPFNet and CE-Net are faster mainly due to custom lightweight encoders, whereas our use of EfficientNet-B4 backbone contributes to the higher FLOPs. Overall, Phi-SegNet maintains competitive runtime efficiency while delivering structurally robust segmentation, validating its practicality among state-of-the-art methods.

VI. LIMITATIONS AND FUTURE WORKS

While Phi-SegNet demonstrates compelling results, several limitations and opportunities remain. The EfficientNet-B4 backbone, though effective for hierarchical representation learning, increases computational and memory demands, constraining deployment in low-resource or real-time settings. Future work may investigate lightweight or compressed variants to improve efficiency. The fixed spectral filter in the RFA modules ($\gamma = 3$) may also limit adaptability across datasets with diverse frequency characteristics; adaptive spectral modulation parameterized by modality or anatomical context could enable data-driven frequency tuning. Furthermore, extending Phi-SegNet to weakly supervised learning and cross-domain adaptation may further enhance robustness and broaden clinical applicability across heterogeneous imaging environments.

TABLE X
ANALYSIS OF PARAMETERS, FLOPS, AND INFERENCE TIME FOR
VARIOUS MODELS WITH INPUT SIZE OF 256 × 256

Methods	#Params	FLOPs	Inference Time
UNet [1]	7.70 M	36.76 G	5.92 ms
UNet++ [5]	9.16 M	34.66 G	7.64 ms
ResUNet++ [36]	4.06 M	15.75 G	7.07 ms
CE-Net [10]	29.01 M	7.16 G	6.99 ms
CPFNet [2]	43.27 M	8.36 G	9.63 ms
PraNet [11]	32.55 M	6.92 G	18.81 ms
Y-Net [37]	7.41 M	13.44 G	8.44 ms
AAU-Net [9]	19.63 M	33.40 G	16.62 ms
MEW-UNet [18]	140.27 M	41.23 G	95.68 ms
TransAttUNet [16]	25.97 M	88.75 G	13.82 ms
Twin-SegNet [13]	71.78 M	16.32 G	22.57 ms
Phi-SegNet	59.72 M	81.91 G	44.41 ms

VII. CONCLUSION

This work presents Phi-SegNet, a CNN-based segmentation framework that integrates phase-aware supervision for enhanced structural delineation. The Bi-Feature Mask Former (BFMF) modules fuse adjacent encoder features to improve semantic coherence, while the Reverse Fourier Attention (RFA) blocks refine decoder representations through phase-regularized features. Extensive evaluations across five imaging modalities confirm Phi-SegNet's consistent state-of-the-art performance, particularly in fine-grained and low-contrast boundaries. Overall, Phi-SegNet reveals how phase-conditioned feature propagation and phase-based supervision can jointly drive more robust segmentation performance, paving the way for deeper integration of signal-level priors into deep learning frameworks for medical imaging.

REFERENCES

- [1] O. Ronneberger, P. Fischer, and T. Brox, "U-net: Convolutional networks for biomedical image segmentation," in *18th International Conference on Medical Image Computing and Computer-Assisted Intervention*, vol. 18, 2015, pp. 234–241.
- [2] S. Feng, H. Zhao, F. Shi, X. Cheng, M. Wang, Y. Ma, D. Xiang, W. Zhu, and X. Chen, "Cpfnet: Context pyramid fusion network for medical image segmentation," *IEEE Trans. Med. Imaging*, vol. 39, no. 10, pp. 3008–3018, 2020.
- [3] A. Srivastava, D. Jha, S. Chanda, U. Pal *et al.*, "MSRF-Net: a multi-scale residual fusion network for biomedical image segmentation," *IEEE J. Biomed. Health Inform.*, vol. 26, no. 5, pp. 2252–2263, 2022.
- [4] X. Zhao, H. Jia, Y. Pang, L. Lv, F. Tian, L. Zhang, W. Sun, and H. Lu, "M2snet: Multi-scale in multi-scale subtraction network for medical image segmentation," *arXiv preprint arXiv:2303.10894*, 2023.
- [5] Z. Zhou, M. M. R. Siddiquee, N. Tajbakhsh, and J. Liang, "Unet++: Redesigning skip connections to exploit multiscale features in image segmentation," *IEEE Trans. Med. Imaging*, vol. 39, no. 6, pp. 1856–1867, 2019.
- [6] J. Schlemper, O. Oktay, M. Schaap, M. Heinrich, B. Kainz, B. Glocker, and D. Rueckert, "Attention gated networks: Learning to leverage salient regions in medical images," *Med. Image Anal.*, vol. 53, pp. 197–207, 2019.
- [7] K. Wang, X. Zhang, X. Lu, S. Huang, and D. Yang, "EANet: Iterative edge attention network for medical image segmentation," *Pattern Recognit.*, vol. 127, p. 108636, 2022.
- [8] A. Sinha and J. Dolz, "Multi-scale self-guided attention for medical image segmentation," *IEEE J. Biomed. Health Inform.*, vol. 25, no. 1, pp. 121–130, 2020.
- [9] G. Chen, L. Li, Y. Dai, J. Zhang, and M. H. Yap, "AAU-net: an adaptive attention U-net for breast lesions segmentation in ultrasound images," *IEEE Trans. Med. Imaging*, vol. 42, no. 5, pp. 1289–1300, 2022.
- [10] Z. Gu, J. Cheng, H. Fu, K. Zhou, H. Hao, Y. Zhao, T. Zhang, S. Gao, and J. Liu, "CE-net: Context encoder network for 2d medical image segmentation," *IEEE Trans. Med. Imaging*, vol. 38, no. 10, pp. 2281–2292, 2019.
- [11] D.-P. Fan, G.-P. Ji, T. Zhou, G. Chen, H. Fu, J. Shen, and L. Shao, "PraNet: Parallel reverse attention network for polyp segmentation," in *23rd International Conference on Medical Image Computing and Computer-Assisted Intervention*, 2020, pp. 263–273.
- [12] J. Li, J. Wang, F. Lin, A. A. Heidari, Y. Chen, H. Chen, and W. Wu, "Prcnet: a parallel reverse convolutional attention network for colorectal polyp segmentation," *Biomed. Signal Process. Control*, vol. 95, p. 106336, 2024.
- [13] S. Ahmed and M. K. Hasan, "Twin-SegNet: Dynamically coupled complementary segmentation networks for generalized medical image segmentation," *Comput. Vis. Image Underst.*, vol. 240, p. 103910, 2024.
- [14] J. Chen, J. Mei, X. Li, Y. Lu, Q. Yu, Q. Wei, X. Luo, Y. Xie, E. Adeli, Y. Wang *et al.*, "TransUNet: Rethinking the U-Net architecture design for medical image segmentation through the lens of transformers," *Med. Image Anal.*, p. 103280, 2024.
- [15] Y. Zhang, H. Liu, and Q. Hu, "Transfuse: Fusing transformers and cnns for medical image segmentation," in *24th International Conference on Medical Image Computing and Computer Assisted Intervention*, vol. 12901, 2021, pp. 14–24.
- [16] B. Chen, Y. Liu, Z. Zhang, G. Lu, and A. W. K. Kong, "Transattunet: Multi-level attention-guided u-net with transformer for medical image segmentation," *IEEE Trans. Emerg. Top. Comput. Intell.*, vol. 8, no. 1, pp. 55–68, 2024.
- [17] A. He, K. Wang, T. Li, C. Du, S. Xia, and H. Fu, "H2Former: An efficient hierarchical hybrid transformer for medical image segmentation," *IEEE Trans. Med. Imaging*, vol. 42, no. 9, pp. 2763–2775, 2023.
- [18] J. Ruan, M. Xie, S. Xiang, T. Liu, and Y. Fu, "MEW-UNet: Multi-axis representation learning in frequency domain for medical image segmentation," *arXiv preprint arXiv:2210.14007*, 2022.
- [19] Y. Chen, X. Zhang, L. Peng, Y. He, F. Sun, and H. Sun, "Medical image segmentation network based on multi-scale frequency domain filter," *Neural Networks*, vol. 175, p. 106280, 2024.
- [20] P. Li, R. Zhou, J. He, S. Zhao, and Y. Tian, "A global-frequency-domain network for medical image segmentation," *Comput. Biol. Med.*, vol. 164, p. 107290, 2023.
- [21] C. Zhu, X. Chai, Z. Wang, Y. Xiao, R. Zhang, Z. Yang, and J. Feng, "Dbl-net: A dual-branch learning network with information from spatial and frequency domains for tumor segmentation and classification in breast ultrasound image," *Biomed. Signal Process. Control*, vol. 93, p. 106221, 2024.
- [22] Y. Li, Z. Zheng, W. Ren, Y. Nie, J. Zhang, and X. Jia, "Dual-domain learning network for polyp segmentation," in *International Workshop on Digital Watermarking*. Springer, 2023, pp. 233–247.
- [23] H. Ding, J. Lu, J. Cai, Y. Zhang, and Y. Shang, "Slf-unet: Improved unet for brain mri segmentation by combining spatial and low-frequency domain features," in *Computer Graphics International Conference*. Springer, 2023, pp. 415–426.
- [24] X. Tang, J. Peng, B. Zhong, J. Li, and Z. Yan, "Introducing frequency representation into convolution neural networks for medical image segmentation via twin-kernel fourier convolution," *Comput. Methods Programs Biomed.*, vol. 205, p. 106110, 2021.
- [25] T. Imtiaz, S. A. Fattah, and S.-Y. Kung, "Bawgnet: Boundary aware wavelet guided network for the nuclei segmentation in histopathology images," *Comput. Biol. Med.*, vol. 165, p. 107378, 2023.
- [26] Q. Van Nguyen, M. Nguyen, T. T. Nguyen, H. T. Quang, T. P. Van, and L. D. Bao, "Lacformer: Toward accurate and efficient polyp segmentation," in *BMVC*, 2023, pp. 411–416.
- [27] M. Tan and Q. Le, "Efficientnet: Rethinking model scaling for convolutional neural networks," in *International Conference on Machine Learning*. PMLR, 2019, pp. 6105–6114.
- [28] W. Al-Dhabyani, M. Gomaa, H. Khaled, and A. Fahmy, "Dataset of breast ultrasound images," *Data in Brief*, vol. 28, p. 104863, 2020.
- [29] K. Panetta, R. Rajendran, A. Ramesh, S. P. Rao, and S. Agaian, "Tufts dental database: a multimodal panoramic x-ray dataset for benchmarking diagnostic systems," *IEEE J. Biomed. Health Inform.*, vol. 26, no. 4, pp. 1650–1659, 2022.
- [30] D. Jha, P. H. Smedsrød, M. A. Riegler, P. Halvorsen *et al.*, "Kvasir-SEG: A segmented polyp dataset," in *26th International Conference on MultiMedia Modeling*, vol. 11962, 2020, pp. 451–462.
- [31] K. Sirinukunwattana, J. P. Pluim, H. Chen, X. Qi *et al.*, "Gland segmentation in colon histology images: The glas challenge contest," *Med. Image Anal.*, vol. 35, pp. 489–502, 2017.
- [32] G. Litjens, R. Toth, W. Van De Ven, C. Hoeks *et al.*, "Evaluation of prostate segmentation algorithms for MRI: The PROMISE12 Challenge," *Med. Image Anal.*, vol. 18, no. 2, pp. 359–373, 2014.
- [33] M. H. Yap, G. Pons, J. Marti, S. Ganau, M. Sentis, R. Zwiggelaar, A. K. Davison, and R. Marti, "Automated breast ultrasound lesions detection using convolutional neural networks," *IEEE J. Biomed. Health Inform.*, vol. 22, no. 4, pp. 1218–1226, 2017.
- [34] P. S. Rodrigues, "Mendeley Breast Ultrasound Image Dataset," Mendeley Data, V1, 2017. [Online]. Available: <https://doi.org/10.17632/wmy84gznwg.1>
- [35] J. Bernal, J. Sánchez, and F. Vilarino, "Towards automatic polyp detection with a polyp appearance model," *Pattern Recognit.*, vol. 45, no. 9, pp. 3166–3182, 2012.
- [36] D. Jha, P. H. Smedsrød, M. A. Riegler, D. Johansen, T. De Lange, P. Halvorsen, and H. D. Johansen, "ResUNet++: An advanced architecture for medical image segmentation," in *2019 IEEE International Symposium on Multimedia*. IEEE, 2019, pp. 225–2255.
- [37] A. Farshad, Y. Yeganeh, P. Gehlbach, and N. Navab, "Y-net: A spatirospectral dual-encoder network for medical image segmentation," in *25th International Conference on Medical Image Computing and Computer-Assisted Intervention*, vol. 13432, 2022, pp. 582–592.